FULL PAPER

High-Mobility Naphthalene Diimide and Selenophene-Vinylene-Selenophene-Based Conjugated Polymer: n-Channel Organic Field-Effect Transistors and Structure–Property Relationship

Min Jae Sung, Alessandro Luzio, Won-Tae Park, Ran Kim, Eliot Gann, Francesco Maddalena, Giuseppina Pace, Yong Xu, Dario Natali, Carlo de Falco, Long Dang, Christopher R. McNeill, Mario Caironi,* Yong-Young Noh,* and Yun-Hi Kim*

Interdependence of chemical structure, thin-film morphology, and transport properties is a key, yet often elusive aspect characterizing the design and development of high-mobility, solution-processed polymers for large-area and flexible electronics applications. There is a specific need to achieve >1 cm^2 V^{-1} s^{-1} field-effect mobilities (μ) at low processing temperatures in combination with environmental stability, especially in the case of electron-transporting polymers, which are still lagging behind hole transporting materials. Here, the synthesis of a naphthalene-diimide based donor–acceptor copolymer characterized by a selenophene vinylene selenophene donor moiety is reported. Optimized field-effect transistors show maximum μ of 2.4 cm^2 V^{-1} s^{-1} and promising ambient stability. A very marked film structural evolution is revealed with increasing annealing temperature, with evidence of a remarkable 3D crystallinity above 180 °C. Conversely, transport properties are found to be substantially optimized at 150 °C, with limited gain at higher temperature. This discrepancy is rationalized by the presence of a surface-segregated prevalently edge-on packed polymer phase, dominating the device accumulated channel. This study therefore serves the purpose of presenting a promising, high-electron-mobility copolymer that is processable at relatively low temperatures, and of clearly highlighting the necessity of specifically investigating channel morphology in assessing the structure–property nexus in semiconducting polymer thin films.

1. Introduction

Over the past two decades, the field of solution-processable organic field-effect transistors (OFETs) has experienced steady progress as a result of the tuning of the electrical properties by chemical synthesis, the control of the microstructure of organic semiconducting films by optimizing deposition processes, and the careful selection of gate dielectrics and charge injection electrode materials with suitable interfacial properties.[1–7] Such progress coupled with the high compatibility of solution-processable organic semiconductors with plastic or metal foil substrates makes them ideal candidates for cost-effective, mechanically flexible electronic devices for various applications, such as printed radio frequency identification tags for item-level tagging, drivers for flexible displays, wearable electronics, distributed sensors, and integrated, nonvolatile memory devices.[8–20] Recently, solution-processed p-type OFETs with

M. J. Sung
School of Materials Science & Engineering and ERI
Gyeongsang National University
501 Jinju Daero, Jinju 660-701, South Korea
Dr. A. Luzio, Dr. F. Maddalena, Dr. G. Pace, Prof. D. Natali,
Dr. M. Caironi
Center for Nano Science and Technology @PoliMi
Istituto Italiano di Tecnologia
Via Pascoli 70/3, 20133 Milan, Italy
E-mail: mario.caironi@iit.it
W.-T. Park, Prof. Y. Xu, L. Dang, Prof. Y.-Y. Noh
Department of Energy and Materials Engineering
Dongguk University
26, Pil-dong, 3-ga, Jung-gu, Seoul 100-715, South Korea
E-mail: yynoh@dongguk.edu
Dr. R. Kim, Prof. Y.-H. Kim
Department of Chemistry and RIGET
Gyeongsang National University
501 Jinju Daero, Jinju 660-701, South Korea
E-mail: ykim@gnu.ac.kr

Dr. E. Gann, Prof. C. R. McNeill
Department of Materials Science and Engineering
Monash University
Wellington Road, Clayton, Victoria 3800, Australia
Prof. D. Natali
Dipartimento di Elettronica
Informazione e Bioingegneria
Politecnico di Milano
Piazza L. da Vinci 32, 20133 Milan, Italy
Prof. C. De Falco
MOX Modeling and Scientific Computing
Dipartimento di Matematica
Politecnico di Milano
Piazza L. da Vinci 32, 20133 Milan, Italy

www.MaterialsViews.com

ADVANCED
FUNCTIONAL
MATERIALS
www.afm-journal.de

FULL PAPER

outstanding charge carrier mobilities have been demonstrated, with the best small molecule and polymer OFETs showing mobilities exceeding 10 cm² V⁻¹ s⁻¹.[21–25] Such remarkable p-channel mobilities, obtained in devices with fairly promising shelf-life and operational stabilities, have been demonstrated with conjugated polymers based on new building units, such as diketopyrrolopyrrole,[24,26,27] isoindigo,[28,29] and indacenodithiophene.[30] Similar efforts have been devoted to improving n-channel polymer semiconductors, with the performances of n-type devices still lagging behind their p-channel counterparts.[31–36] The main obstacle that has traditionally prevented the improvement of electron transporting polymers is the presence of trap sites forming at around −3.8 to −4.0 eV, mainly associated with hydrogenated oxygen, which complicates the design of conjugated polymers because of the requirement for a lowest unoccupied molecular orbital (LUMO) energy level that lays below this range.[37] In the recent past, different solutions have been proposed, among which a remarkably well performing solution-processable n-type polymer reported by Yan et al., based on a naphthalene diimide (NDI) acceptor moiety (referred to as PNDI2OD-T2) and easily achieving field-effect mobilities in the 0.1 to 1 cm² V⁻¹ s⁻¹ range, represented a breakthrough in the development of n-channel organic polymeric semiconductors.[38] The two strong electron-withdrawing imide groups per naphthalene unit can effectively pull down the LUMO energetic level, leading to improved air stability. The electron-deficient NDI center implements a bicyclic planarization within the conjugated structure, intended to provide a strong π–π interaction and hence efficient interchain transport of intrachain localized carriers throughout the film.[39] Furthermore, the ease of functionalization at the N-position of the imide ring with different substituents enables control of the physical properties such as solubility, crystallization, air stability, and self-assembly.[40,41] More recently, improved electron mobilities could be achieved by acting on the donor unit in a NDI-based copolymer. In particular, an electron mobility of ≈1.5 cm² V⁻¹ s⁻¹ was achieved by copolymerization of a long alkyl substituted-NDI unit with a bithiophene end-capped thienylene-vinylene-thienylene unit (PNDI-TVT).[42]

Alternative opportunities for the basic structure of the donor moiety stem from synthetic efforts that have in the past been directed at replacing thiophene units with electron-rich selenophenes, with the purpose of enhancing the intermolecular interactions and thus interchain charge transfer with respect to thiophene analogues.[43–46] Such a path has led various research groups to demonstrate high-mobility p-channel conjugated polymers with improved ambient stability.[44,47–51] Despite the strong interest in the incorporation of selenophenes in p-channel conjugated polymers, their use in n-channel and/or ambipolar polymers has been quite limited so far.[52]

While the chemical structure of the polymer semiconductor is of fundamental importance in determining the optoelectronic properties of a material, it is also very well known that in the solid state the film morphology and the packing motif of the conjugated segments critically size the charge transport properties.[1,2] For example, control of the alignment of the polymer backbones in a thin film can strongly enhance the charge carrier mobility.[53–57] In the case of the model n-type polymer PNDI2OD-T2, an electron mobility exceeding 6 cm² V⁻¹ s⁻¹ at high fields was achieved with a fast bar-coating process, starting from solutions with a high degree of preaggregation, leading to aligned fibrillar domains over large areas[3] as a result of flow induced alignment, achievable with an off-center spin-coating process as well.[58,59]

Such results indicate the beneficial interplay of chemical structure and solid-state morphology in improving charge transport properties, a common aspect of solution-processed high-mobility polymers typically indicated as the structure–property nexus. This relationship has not been fully resolved yet, and while the bulk film microstructure is most typically correlated with transport properties, elusive and sometime contradictory aspects have recently induced researchers to investigate more closely the so-called functional morphology, i.e., the morphology of the only volume of the film that is involved in charge transport within the nanometer-thick accumulated channel of a FET.[60–62]

In this contribution, we fulfill the double aim of reporting the synthesis of a new and high-electron-mobility NDI-based copolymer, incorporating a selenophene-vinyl-selenophene donor moiety, and of evidencing a clear deviation between channel and bulk film morphology. First, we report on the synthesis and full characterization in an OFET device configuration of the solution-processed polymer poly[(E)-2,7-bis(2-decyltetradecyl)-4-methyl-9-(5-(2-(5-methylselenophen-2-yl)vinyl)selenophen-2-yl)benzo[lmn][3,8] phenanthroline-1,3,6,8(2H,7H)-tetraone] (PNDI-SVS, **Scheme 1**). OFET devices based on this new copolymer are characterized by high electron mobility, exceeding 2.4 cm² V⁻¹ s⁻¹, with a promising
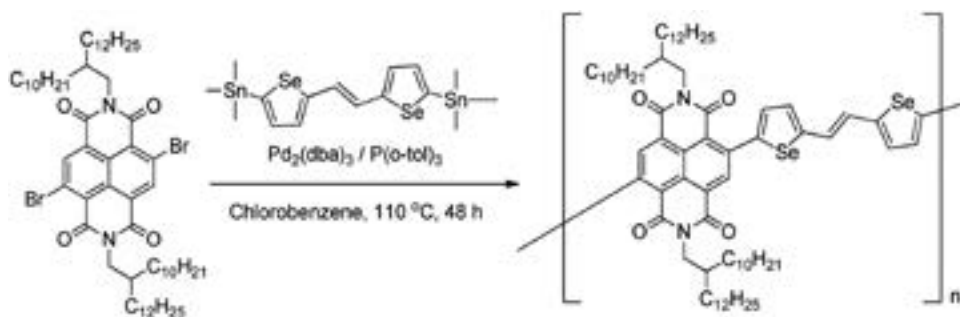
Scheme 1. Synthesis of poly[(E)-2,7-bis(2-decyltetradecyl)-4-methyl-9-(5-(2-(5-methylselenophen-2-yl)vinyl)selenophen-2-yl)benzo[lmn][3,8] phenanthroline-1,3,6,8(2H,7H)-tetraone], PNDI-SVS in short.

FULL PAPER

Table 1. Physical properties of PNDI-SVS.

Polymer	Yield [%]	M_n/M_w [kDa]	λ_{abs} [nm]		T_d [°C]	LUMO[a] [eV]	HOMO[b] [eV]	E_g [eV]
			Solution	Film				
PNDI-SVS	97	80/168	403, 711	416, 748	387	−3.98	−5.29	1.31

[a]$E_{LUMO} = -(E_{1/2}^{red-1} + 4.43 \text{ eV})$; [b]$E_{HOMO} = E_{LUMO} - E_g$ (estimated from optical absorption spectrum).

ambient-air operational stability. We then thoroughly investigate the microstructure of PNDI-SVS thin films as a function of annealing temperature by means of grazing incidence wide angle X-ray scattering (GIWAXS), showing a marked evolution toward a more crystalline phase with temperatures up to 180 °C, where a remarkable 3D crystal structure arises. Interestingly, very good electron mobility can be achieved already at low processing temperatures (150 °C), highly favoring application of the copolymer in plastic-based flexible circuits. This apparently contradictory result is rationalized through a deep analysis of the micro and electronic structure within the few nanometers-thick accumulated channel at the semiconductor–dielectric interface thanks to near edge X-ray absorption fine structure (NEXAFS) spectroscopy, extraction of the effective density of states, and charge modulation micro-spectroscopy.

2. Results

2.1. Synthesis and Density Functional Theory Calculation

PNDI-SVS was synthesized by a Stille coupling reaction using Pd$_2$(dba)$_3$ and P(o-Tol)$_3$, as shown in Scheme 1. The polymer was extracted with chloroform, collected by precipitation in methanol, and purified by successive Soxhlet extractions using methanol, acetone, toluene, and chloroform to remove biproducts and oligomers. The chemical structure of the obtained PNDI-SVS was confirmed by ^{1}H NMR (Figure S1, Supporting Information). The PNDI-SVS is soluble in common organic solvents, notably chloroform and chlorobenzene. The molecular weight of the polymer was determined by gel permeation chromatography (GPC) with polystyrene standards in chloroform (see Figure S2, Supporting Information). An average molecular weight (M_n) of 80.0 kg mol^{-1} and a weight average molecular weight (M_w) of 168.0 kg mol^{-1}, with a polydispersity index of 2.1, were found. Such a high molecular weight was achieved owing to the good solubility in common solvents.

The optical absorption of a PNDI-SVS chloroform solution and thin film deposited from spin coating is shown in Figure S3a of the Supporting Information. PNDI-SVS absorption spectra are characterized by absorption maxima at 403 and 711 nm in solution, and at 416 and 743 nm in the solid state. Analogously with previous reports on PNDI2OD-T2, the two distinctive peaks observed can be attributed to a π–π* transition and an intramolecular transition with charge transfer character between the electron-donating unit and the electron-acceptor unit, respectively.[63–67] With respect to the analogue NDI copolymer with the thienylene moiety instead of the selenophene, PNDI-SVS UV–vis absorption maxima are 30 nm red shifted owing to the introduction of a slightly stronger electron donor unit. Correspondingly, the optical band gap

of PNDI-SVS, estimated at the onset of absorption maxima, is 1.31 eV, slightly narrower than the bandgap of PNDI-TVT. This is presumably owing to the extended π-conjugation achievable through the introduction of the electron-rich SVS moiety. As shown in Figure S3b of the Supporting Information and **Table 1**, from cyclic voltammetry measurements, the estimated LUMO energy of PNDI-SVS is −3.98 eV. The LUMO energy of PNDI-SVS is slightly lower than that of the well-known NDI polymer PNDI2OD-T2 (−3.91 eV), a variation in the direction of improved air stability.[63] The thermal properties of the polymer were studied by carrying out thermogravimetric analysis (TGA) and differential scanning calorimetry (DSC). PNDI-SVS showed good thermal stability, with weight losses stating at 387 °C in the TGA measurements (Figure S4, Supporting Information). PNDI-SVS showed no glass transition in the temperature range of 50—250 °C in the DSC thermograms (Figure S4, Supporting Information).

Density functional theory (DFT) calculations were also carried out at the B3LYP 6–31G** level. As expected, the coefficients of the HOMO orbital are located on the SVS unit while that of the LUMO orbital is mainly positioned on the NDI unit, in good agreement with other NDI derivatives (Figure S5, Supporting Information).[31,67] The dihedral angles between the NDI and SVS units are 47.70° and 43.78° (Figure S5b, Supporting Information), which are larger than those reported for NDI and TVT, and NDI and bithiophene units, being 33.44° and 32.82°, and 32.88° and 40.61°, respectively.[66,68,69] The difference between the dihedral angles of these copolymers suggests a clear departure from extensive and continuous planarity in the polymer films with the most distorted being the PNDI-SVS copolymer. Physical properties, including optical bandgap, and HOMO and LUMO energetic levels, are summarized in Table 1.

2.2. Structural Characterization of Thin Films

In order to investigate the microstructure of the PNDI-SVS thin films, we performed GIWAXS on a series of samples annealed for 20 min at different temperatures up to 250 °C and for a sample annealed for 24 h at 130 °C. The 2D GIWAXS patterns are shown in **Figure 1**.

Increased annealing temperature decreases the orientational disorder within the films, making the peaks narrower azimuthally. While up to 150 °C the films show largely liquid crystallinity with scattering peaks only clearly in-plane and out-of-plane, for $T \geq 180$ °C there is clear evidence for 3D crystallinity, with several mixed-index peaks (away from the vertical and horizontal axes) evident.

For $T \leq 210$ °C and an annealing duration of 20 min, the 2D scattering patterns indicate a generally face-on orientation with
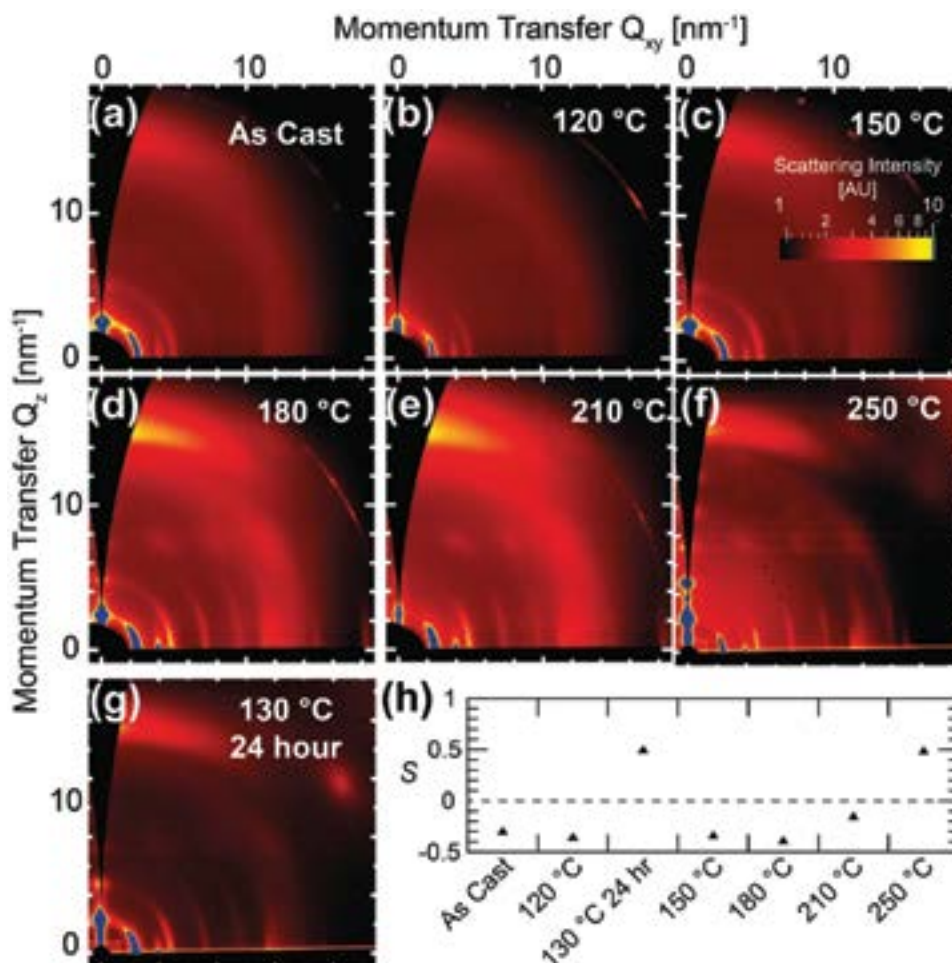
www.MaterialsViews.com

ADVANCED
FUNCTIONAL
MATERIALS
www.afm-journal.de

FULL PAPER

Figure 1. 2D GIWAXS patterns plotted versus in-plane and out-of-plane momentum transfer (Q_{xy} and Q_z, respectively) for a) as cast, b) 120 °C 20 min, c) 150 °C 20 min, d) 180 °C 20 min, e) 210 °C 20 min, f) 250 °C 20 min, and g) 130 °C 24 h. h) Herman's orientational parameter (S) calculated from the polar distribution of the second order alkyl stacking peak, plotted versus annealing temperature.

alkyl stacking lamella peaks largely in-plane and π-stacking peaks predominantly out-of-plane. At both higher temperatures (250 °C) and longer annealing times, a clear out of plane alkyl stacking peak, dim in the other scattering patterns, becomes quite evident, indicating an edge-on realignment in the film.

To quantify the overall orientation of crystallites within the thin films, we calculated Herman's orientational parameter (S) using previously established methods.[70] A value of $S = 1$ indicates a film consisting of perfectly aligned edge-on crystals, while a value of −0.5 indicates perfect face-on stacking within the film. Up to 180 °C at 20 min of annealing, S progressively decreases with increasing temperature from −0.3 to −0.4, indicating mostly face-on crystalline orientation and a narrowing of the distribution width, matching the narrowing polar distribution we see in the 2D scattering patterns. At 210 °C, however, S increases to −0.2 and finally switches to a positive value of 0.5 at 250 °C, indicating a significant edge-on component at 210 °C, which becomes the predominant stacking orientation within the film at 250 °C. Similar edge-on predominance is seen at longer annealing times in the film annealed for 24 h at 130 °C, indicating that the edge-on orientation is energetically

preferred even at lower temperatures, which may require more time for large-scale realignment and propagation throughout the film owing to lower mobility.

To examine the crystalline parameters more carefully, in-plane and out-of-plane sector profiles were calculated, as shown in **Figure 2**.

The three unit cell directions are identified as an alkyl stacking from backbone to backbone across the alkyl side chains ($\approx$2.6 nm), from backbone to backbone in a π-stack (0.41 nm), and from one monomer to the next along the backbone (1.6 nm), which are labeled in the 1D sector profiles in Figure 2. Upon annealing initially to 120 °C for 20 min, we see a general loss of crystallinity and a decrease of coherence length, indicating that at this low temperature (and short annealing time), the crystals that were formed upon casting are disrupted slightly. Upon annealing at 180 °C for 20 min, we can see that in all unit cell directions, both the coherence length and the relative crystallinity increase considerably. Upon annealing at 210 °C for 20 min, while the crystallinity remains high and even increases, the coherence length of those crystals decreases slightly, as this is the temperature at
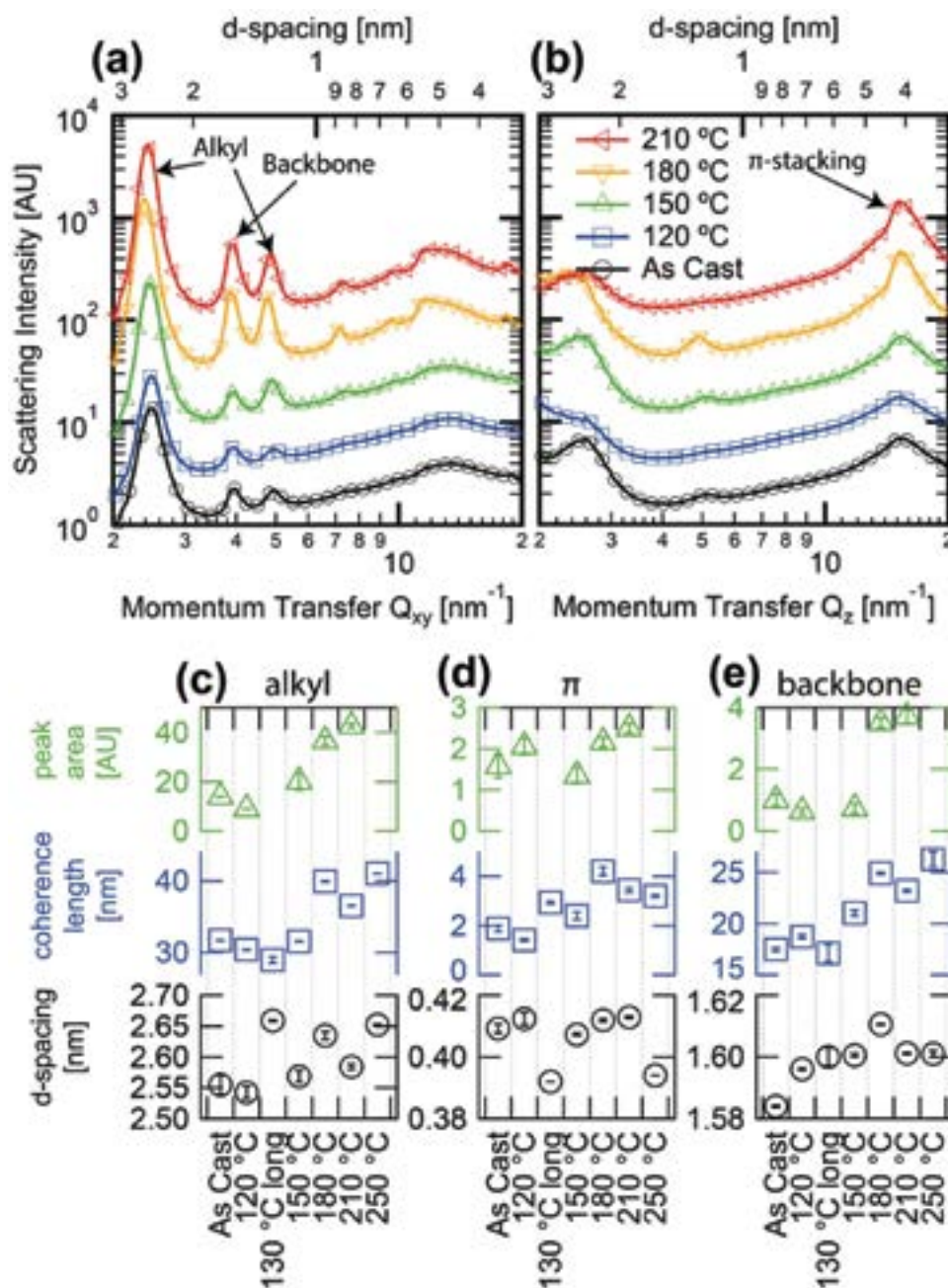
Figure 2. 1D 15° sector profiles calculated from the 2D GIWAXS patterns. a) Scattering intensity versus in-plane momentum transfer Q_{xy}. b) Scattering intensity versus out-of-plane momentum transfer Q_z. Peak fitting results are displayed for c) the alkyl stacking peak, d) the π-stacking peak, and e) the peak corresponding to the repeat unit along the conjugated backbone versus temperature. The corresponding peaks are labeled in (a) and (b).

which the molecular packing orientation was seen to begin to change. Note that because of the large-scale realignment of the film at 250 °C and for the longer anneal at 130 °C, many of the crystalline planes that contribute to each peak are scattering to different directions, making it quite difficult to compare the peak area and spacing accurately to those at the lower temperatures/shorter annealing times. We can however see that the coherence length remains at about the same level, and there is no indication of a drastically different unit cell.

Subtle changes to the unit cell are evident upon annealing, with the alkyl stacking distance and backbone repeat distance increasing up to 180 °C, which indicates a straightening of the backbone and alkyl side chains. Meanwhile, the π-stacking distance remains largely unchanged. Upon annealing to 210 °C, the unit cell dimensions reduce once again. We speculate that the large crystals with straightened backbone obtained at 180 °C are no longer stable at 210 °C, as the film begins to reorient. At higher temperatures, crystallinity is high once again, indicating that after reorientation, crystals can again grow freely.

www.MaterialsViews.com

ADVANCED
FUNCTIONAL
MATERIALS
www.afm-journal.de

FULL PAPER

Long-duration annealing at low temperature (130 °C, 24 h), as previously noted, leads to similar crystalline structures and orientations as those found at higher temperatures for shorter times (250 °C, 20 min), revealing no evidence of a phase transition for T ≤ 250 °C. The one difference in the crystalline structure is that the coherence lengths along all directions are much higher in the high-temperature annealed film, indicating that the quality and size of the crystallites are improved when using high-temperature short-duration thermal treatments rather than low-temperature long-duration treatments.

To investigate the overall alignment of the backbone, both at the surface and within the bulk of the polymer, near edge X-ray absorption fine structure (NEXAFS) spectroscopy was collected on films where a largely face-on bulk orientation was demonstrated by GIWAXS measurements, i.e., as-cast, 120 °C 20 min, 150 °C 20 min, 180 °C 20 min, and 210 °C 20 min. The total electron yield (TEY) results are presented in **Figure 3**, along with the tilt angles determined through TEY, partial electron yield (PEY), and fluorescence yield (FY).

PEY is the most surface-sensitive of the techniques, measuring the upper 1–3 nm of the film. TEY is also surface-sensitive, although it is sensitive to the upper 2–5 nm of the film. FY is bulk sensitive, measuring the entirety of the thin film. All tilt angles are calculated from a peak fit of structure at lower energies than 286 eV, which is in the π^* manifold, corresponding to transition dipole moments normal to the face of a conjugated core, along the direction of the carbon π orbitals. The NEXAFS tilt angles for the as-cast films show a marked difference between the surface layer, as revealed by PEY and TEY, and the bulk of the thin films, as revealed by FY. At the surface, tilt angles are consistently more edge-on than within the bulk. Annealing at 150 and 180 °C produces the highest edge-on orientation, with the highest tilt angle being 63.6° at 150 °C. Further annealing to 210 °C decreases the surface tilt angle back toward 55°. The bulk of the films maintain a highly face-on orientation, with a general decrease in this orientation upon annealing consistent with the GIWAXS results.

Although beyond the scope of this paper, we want to note here that through careful angle-dependent GIWAXS measurements and analysis, a crystalline self-stratification effect was observed in the film annealed to 210 °C for 20 min. This resulted in a 9 nm edge on-crystalline region lying on top of a 63 nm face-on crystalline region. This surface orientational segregation matches the overall orientational difference we measure in NEXAFS, and provides evidence that this surface region is crystalline. Details and further discussion are reported in a separate work.[71] AFM investigation of PNDI-SVS films revealed a textured topography composed of elongated structures, common to both as-cast and annealed films (210 °C, 20 min) (**Figure 4**). Such topographic features are usually observed in the parent polymer P(NDI2OD-T2) and they have been ascribed to self-assembling phenomena occurring during film deposition and solidification and just initiated by aggregates present in solution;[3] this correspondence with P(NDI2OD-T2) morphology is also reflected by GIWAXS, revealing a mostly face-on stacking in the bulk, and by NEXAFS, evidencing a pronounced edge-on molecular arrangement at the surface.[72] In the case of the as-cast film (Figure 4a) (R_{rms} = 0.7 nm), topographic features are many tens of nm wide (up to 40 nm), while their length is inaccessible, with the elongated structures being mostly intertwined and interconnected to each other; however, segments up to 500 nm long with coherent directionality can be observed. From the section analysis of those nanostructured segments that are less woven and more clearly stacked (Figure 4b), thickness values of ≈2.3–2.9 nm were extracted, thus in good agreement with a mostly edge-on orientation. The sample annealed at 210 °C (Figure 4c) displays a slightly rougher surface (R_{rms} = 0.9 nm), likely reflecting the enhanced crystallinity of the film, in which the elongated microstructures appear much more fused one into another. The section analysis of such a top layer is accessible through discontinuity regions (Figure 4d),
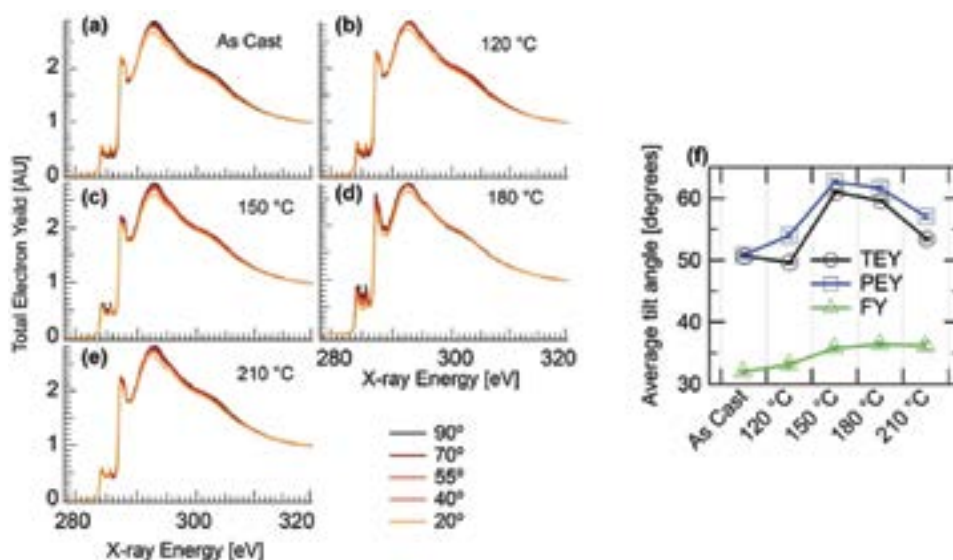

Figure 3. The NEXAFS results of PNDI-SVS films upon annealing. TEY spectra across the Carbon 1S absorption edge are shown for a) as cast and b) 120 °C, c) 150 °C, d) 180 °C, and e) 210 °C annealed films. f) A summary of the tilt angles measured from TEY, PEY, and FY NEXAFS data.
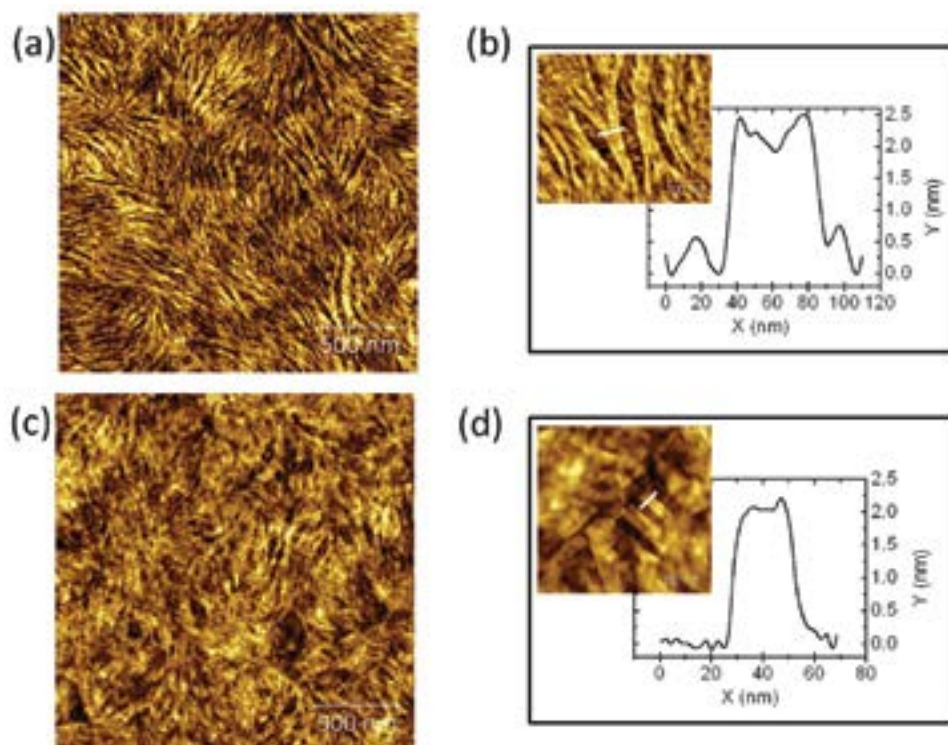
FULL PAPER

Figure 4. a,c) AFM image images and b,d) section analysis of superficial nanostructures of (a,b) PNDI-SVS as-cast film and (c,d) film annealed at 210 °C.

revealing its monomolecular nature and slightly inferior thickness values compared to the nanostructures observed in the topography of the as-spun sample (≈2.0–2.6 nm), which is again in agreement with the reduction of the tilt angle predicted by NEXAFS on the same sample.

It is worth highlighting that a clear discrepancy between bulk (observed by GIWAXS and FY NEXAFS) and top surface (observed by PEY, TEY NEXAFS, and AFM) structural evolution with temperature was observed: the first one showing a clear transition from mostly face-on to largely edge-on crystallite orientation, the second one displaying a majority of edge-on molecular orientation already in as-cast films and maximum tilt angle values for films annealed around 150–180 °C. Therefore, it is possible that there is a subtle surface reconstruction with annealing that is not discernible with GIWAXS and whose structure is hard to elucidate with NEXAFS, but which is clearly suggested by topographic investigation.

2.3. Electrical Characterization of FET Devices

We fabricated top-gate, bottom-contact PNDI-SVS FETs using poly(methyl methacrylate) (PMMA, ε = 3.6) (**Figure 5** and **Table 2**) as the dielectric layer. All the FETs exhibited typical ambipolar characteristics, with high electron mobility and low hole mobility. Generally, an incremental enhancement of the source to drain electron current (I_{DS}) with temperature is observed when the semiconductor undergoes 20 min thermal annealing in nitrogen atmosphere (**Figure 6**a): correspondingly, we have

extracted increasing electron mobility values (μ_e) at V_{GS} = V_{DS} = 60 V, going from the pristine (as cast) film ($\mu_e \approx$ 0.1 cm^2 V^{-1} s^{-1}) up to films annealed at T = 150 °C, reaching mobility values eventually superior to 2.0 cm^2 V^{-1} s^{-1}. Annealing at temperatures higher than 150 °C does not provide substantial improvement of the OFETs performances, however a reduction of threshold voltages can be observed, allowing an average μ_e of 2.4 cm^2 V^{-1} s^{-1} to be achieved (T = 250 °C). The introduction of a very thin injection/doping layer of Cs$_2$CO$_3$[73,74] between the source and drain electrodes and PNDI-SVS film results in $\mu_e \approx$ 0.5 cm^2 V^{-1} s^{-1} using as cast films (Figure S6, Supporting Information); thus, already five times higher mobilities can be achieved without necessarily taking advantage of a thermally induced structural reorganization of the as-cast polymeric films.

Another major point of concern for the practical use of polymeric OFETs is the ambient stability, especially in the case of n-type polymers.[75] Device instabilities are usually observed in the form of hysteretic transfer curves, accompanied by a gradual decrease in the channel current under constant bias conditions, when operated in ambient air without encapsulation. This latter occurs as a consequence of a shift in the threshold voltage (V_{th}) and also of a drastic reduction of the charge carrier mobility. To check the ambient and bias stress stability of PNDI-SVS FETs, we measured the FET characteristics of as-cast (Figure S7, Supporting Information) and 210 °C annealed films under continuous switch on and off in air at a constant gate voltage (V_{GS} = 60 V) for more than 8 h (Figure 5c) and under continuous biasing at constant V_D = 30 V and V_G = 60 V for 2 h (Figure 5d, Supporting Information). Both the on and off currents remained
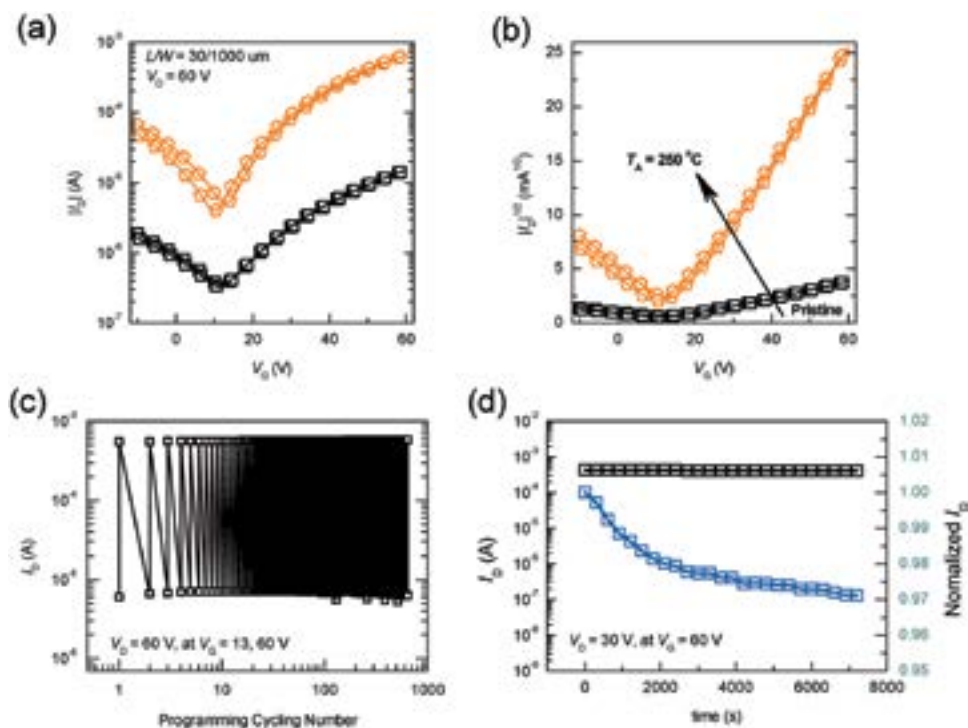
www.MaterialsViews.com

ADVANCED
FUNCTIONAL
MATERIALS
www.afm-journal.de

FULL PAPER

Figure 5. a) Transfer characteristics of PNDI-SVS OFETs (L/W = 30 μm/1 mm) fabricated as cast (black) and annealed at 250 °C (orange) and b) square root drain current curves. c) Programming cycling test with continuous V_D (= 60 V) bias and switched V_G bias (off at 12 V, on at 60 V). d) Bias stability result under continuous bias conditions (V_D = 30 V, V_G = 60 V) depending on time (210 °C annealed OSC).

substantially constant upon on–off cycling (Figure S7a, Supporting Information and Figure 5c) and a constant biasing in air resulted in just a 3% reduction of the on current after 2 h in the case of 210 °C annealing (Figure 5d) and an 18% reduction in the as cast film (Figure S7b, Supporting Information), suggesting in both cases a stable device threshold voltage and quite unmodified transport characteristics throughout both the stress tests. The stability of PNDI-SVS OFET is thus similar to other air-stable NDI copolymers with extended donor unit, such as PNDI-TVT, and apparently improved when compared to the parent PNDI2OD-T2 with bithiophene donor; while the relatively low LUMO energetic value (−3.98 eV) of the polymer may

have resulted in reduced electron transfer phenomena, which can initiate NDI degradation,[76] the comparison between the as-cast and the annealed films highlights the contribution of the superior crystallinity in improving electrical stability in air, likely owing to a more efficient protection of the polymeric charged

Table 2. Device parameters of PNDI-SVS OFETs with various annealing conditions (W/L = 1 mm/30 μm).

Annealing temperature (T_A) [°C]/[min]	S/D electrode	$\mu_{e,sat}$ [cm² V⁻¹ s⁻¹]	$V_{e,Th}$ [V]	S.S. [V dec⁻¹]
Pristine	Au	0.1 (± 0.02)	12.2 (± 1.1)	20.0 (± 0.7)
	Cs₂CO₃/Au	0.5 (± 0.15)	7.1 (± 1.5)	4.3 (± 0.6)
120/20	Au	0.3 (± 0.08)	19.9 (± 1.1)	16.26 (± 1.2)
150/20	Au	1.9 (± 0.22)	18.2 (± 0.7)	16.1 (± 1.1)
180/20	Au	1.9 (± 0.54)	17.1 (± 0.7)	12.3 (± 0.6)
210/20	Au	2.2 (± 1.01)	16.4 (± 0.8)	14.5 (± 1.3)
250/20	Au	2.4 (± 0.39)	14.6 (± 1.0)	10.0 (± 0.2)

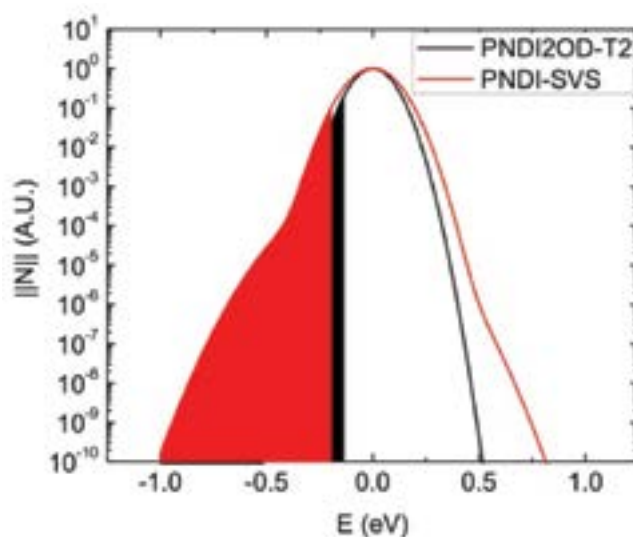**Figure 6.** The DOS of PNDI2OD-T2 (black) and PNDI-SVS (red) annealed at 120 °C (black). The shaded areas represent the filling of the DOS at V_G = 60 V.

core from the contact with oxygen and water, operated through the branched hydrophobic side chains.

2.4. Electronic Structure

To assess the electronic structure of PNDI-SVS, we adopted a methodology to extract the density of states (DOS) using Metal Insulator Semiconductors (MIS) structures.

Maddalena et al. recently developed a tool of general applicability which is based on populating and probing the DOS in the quasi-static regime by means of capacitive coupling in MIS structures.[62] The main advantage with respect to other electrical techniques lies in the fact that by operating the MIS in the quasi-static regime carrier transport is not involved; hence, the DOS can be investigated without making hypotheses or assumptions on the charge transport model.

Experimental capacitance–voltage (CV) characteristics of MIS devices are fitted assuming that the DOS can be modeled as a superposition of Gaussian functions, each characterized by its own width (σ) and number of states (N_0).[62] For films subjected to 18 h of thermal annealing at 130 °C after deposition, our best fit yields an effective DOS composed of two Gaussian functions, a main one and a secondary, smaller, intragap one. For the main one, the center was set at the polymer LUMO level, $N_{0,1}$ was set to 10^{21} cm^{-3}, and the best fit was obtained using $\sigma_1 = 92$ meV. For the secondary Gaussian, best fits were obtained shifting its center by 0.1 eV with respect to the main one and using $N_{0,2} = 10^{18}$ cm^{-3} and $\sigma_2 = 161$ meV. The fitted DOS is plotted in Figure 6, where the shaded areas represent the filling of the DOS at a gate voltage of 60 V. The total concentration of charge carriers at 60 V is of 1.6×10^{19} cm^{-3}. The same method employed to extract the DOS of the parent polymer PNDI2OD-T2, results in a single Gaussian function with a width of 78 meV,[62] much narrower than PNDI-SVS films optimized for transport.

The secondary Gaussian of PNDI-SVS might be related to intragap, low mobility states. As for the main PNDI-SVS Gaussian, it might be surprising that its width is larger than PNDI2OD-T2, given the fact that PNDI-SVS carrier mobility is higher (a DOS comparison is shown in Figure 6). To reconcile these aspects, we can speculate that PNDI-SVS DOS is spatially correlated.[77] In fact, as far as carrier mobility is concerned, spatial correlation can counterbalance energetic disorder because it makes the energy level landscape smoother with respect to the uncorrelated case. Hence, we show that a broadening of the effective DOS does not necessarily imply a poorer charge transport, as may be assumed, and a strong influence of morphological factors should necessarily be taken into account to properly model the transport properties of a polymeric channel.

2.5. Polarized Charge Modulation Microscopy

From the electrical characterization of the FETs reported in the previous section, a major point regarding the functional microstructure–properties nexus arises: low-temperature annealed films (150 °C) display electron transport properties comparable to films that underwent strong structural

rearrangement through higher-temperature thermal annealing. Thus, a correlation between structure and mobility (as calculated from a FET) or DOS (as extracted from MIS structures) cannot be easily traced. When trying to establish such a nexus, we have first to take into account that, in FETs in full accumulation, charges probe only a few nm-thick semiconductor layer at the interface with the dielectric, and this critical region may display a different microstructure from the bulk.[72] Moreover, charge transport in organic semiconductors not only depends on features like crystallinity, but, especially in films with a consistent amorphous-like phase, important factors are also film interconnectivity[1,78] and degree of non-crystalline orientational order,[79] as recently evidenced for example for PNDI2OD-T2.[3,80] Therefore, typical bulk average structural characterization of the ordered phase, as obtained by GIWAXS, has to be completed with more specific, channel sensitive investigations. For the PNDI-SVS copolymer investigated in this work, AFM surface analysis and surface-sensitive NEXAFS reveal that the packing motif at the surface of the film is prevalently edge-on, compared to the prevalently face-on packing of the bulk. Moreover, angle-dependent GIWAXS measurements have highlighted a stratification effect resulting in a 9 nm edge-on crystalline region lying on top of a 63 nm face-on crystalline region.[71] It therefore becomes essential to selectively analyze the functional morphology of the accumulation channel of films in actual devices and to directly image the charge distribution along the channels of working devices. We previously showed that charge modulation microscopy (CMM)[61] probes only those mobile charges accumulated at the gate dielectric. Therefore, only charged conjugated segments which can be populated and depopulated at the gate bias frequency modulation can be imaged. Furthermore, when a polarized light is used for the probing beam (p-CMM), the angular mapping of the in-plane component of the transition dipole moment (TDM) of the charge-induced optical transitions is also possible. In previous work it has been shown that the TDM can be also related to the preferential in-plane alignment of the polymer backbone.[60]

Before proceeding with the charge modulation mapping, we acquired the charge modulation spectra (CMS) of PNDI-SVS (Figure S8, Supporting Information), which is overall red-shifted with respect to the one of PNDI2OD-T2, reflecting the smaller band-gap. Both spectra show two peaks in the ground state absorption bleaching region ($\Delta T/T > 0$), and one polaronic absorption peak ($\Delta T/T < 0$). Such features have been previously assigned.[39]

According to the observed CMS spectra, we performed the charge modulation mapping by probing the samples at 745 nm in correspondence with the bleaching signal of the main absorption peak. The CMM data acquired on PNDI-SVS FETs annealed at 120° (20 min), 250° (20 min) and as-cast in the presence of Cs_2CO_3 as the injection layer, are presented in **Figure 7**. The orientation maps found per each device treatment (Figure 7a–c) represent the average TDM angular orientation of the bleached ground state absorption, i.e., the average orientation along the channel area of polymer backbones where mobile charge resides. We also report the degree of order (DO) maps in Figure 7d–f. The DO corresponds to the ratio between the light polarization-dependent signal and the total charge
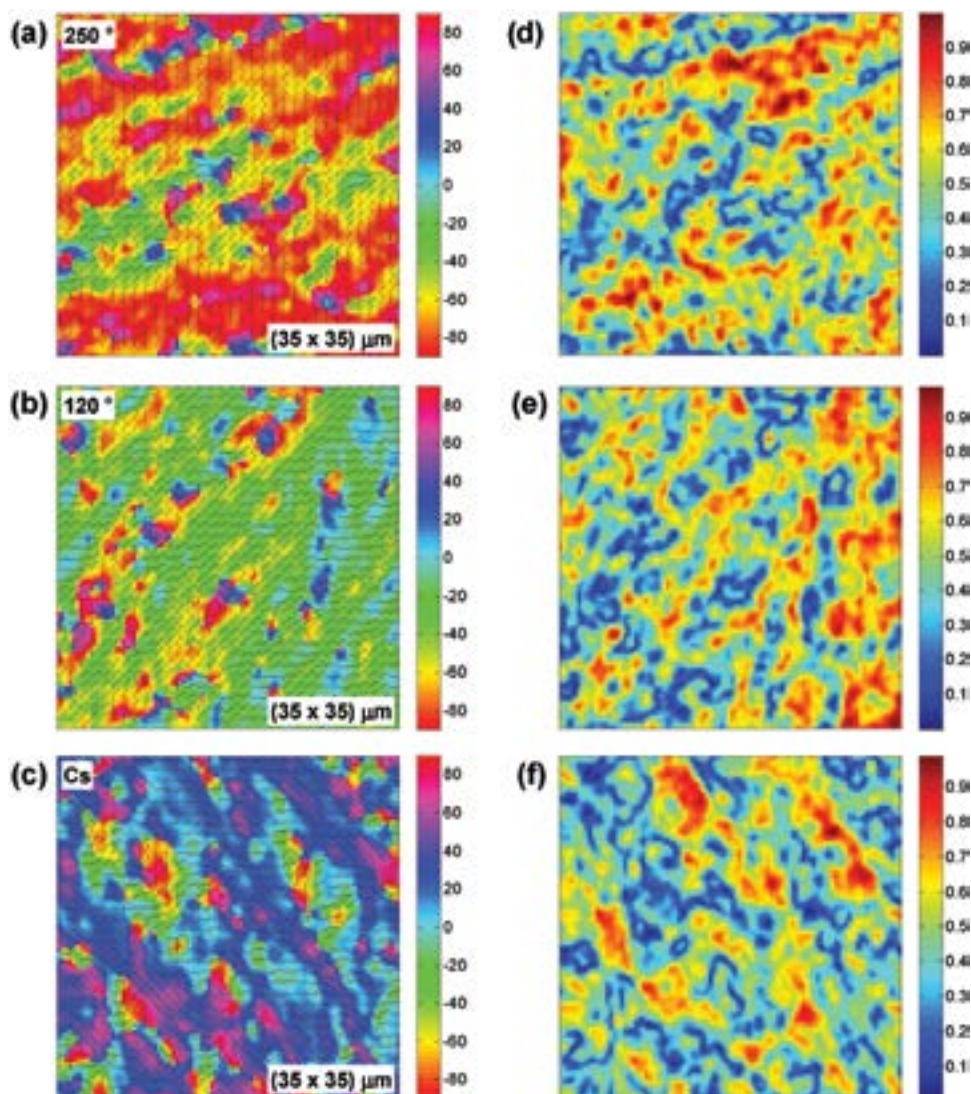
www.MaterialsViews.com

ADVANCED
FUNCTIONAL
MATERIALS
www.afm-journal.de

FULL PAPER

Figure 7. CMM maps of the angle orientation of the charge transition dipole moment measured on PNDI-SVS-FET (V_g = 40 V; V_{pp} = 40 V; modulation frequency 989 Hz): a) FET with semiconductor film annealed at 250 °C, 20 min; b) annealed at 120 °C, 20 min; c) as-cast with Cs salt. On the right the degree of order maps corresponding respectively to d) 250 °C, e) 120 °C, f) as-cast with Cs salt. The source and drain electrode are at the left and right sight of the scan area. The maps are reproducible over different sampling areas.

modulation signal, indicating the fraction of the signal arising from aligned TDM.[60]

In all maps, clear orientational domains of the optical dipoles can be observed, likely sustained by the fibrillar-like supramolecular morphology observed with AFM at the top surface of the films. According to the maps, charge is probing orientational domains with a limited spatial extent (hundreds of nanometers), with a largely variable orientation in the mapped area and with only a slight orientational coherence in the long-range. Importantly, from each map, average degree of order values of 48%, 44%, and 51% were calculated for 120 °C, as-cast on Cs_2CO_3, and 250 °C samples, respectively. As a comparison, in the case of the parent PNDI2OD-T2, a clear correlation between transport properties and orientational order was observed with p-CMM:[60] when a high degree (≈100%) of order is achieved, mobility superior to 1 cm^2 V^{-1} s^{-1} is measured, while cases of

lower degree of order, similar to that observed in PNDI-SVS, lead to mobilities of ≈0.1 cm^2 V^{-1} s^{-1}. In the case of PNDI-SVS, maps are found to be quite invariant with thermal treatments both in terms of orientation and degree of order. This is clear evidence that thermal treatment only is not active on the orientational order of the functional phase of the polymer and that the strong bulk morphological rearrangements observed with GIWAXS is not reflected in the FET channel orientational morphology of PNDI-SVS films. Conversely, CMM maps are in agreement with the quite invariant orientational arrangement of the molecules in the top layers of the film observed with NEXAFS measurements.

Despite the similar CMM maps, the investigated films have shown quite different charge transport properties, the film annealed at high temperature displaying higher mobility values than the as-cast and the 120 °C annealed films (see Table 2).

Part of the increase can be attributed to a more efficient charge injection, since a five times higher mobility is observed already in as-cast samples with the insertion of a thin Cs_2CO_3 charge injection layer. However, there is a further increase of approximately a factor of four for temperatures >150 °C, which has to derive from improved transport properties. Since the micrometric orientational domains displayed by CMM are already present in low-temperature films, the bottleneck for charge transport cannot be found on such length scale. The improved transport therefore has to derive from a finer microstructural evolution, where already for annealing temperatures superior to 120 °C, a packing reorganization favors a more efficient interchain transport and domains interconnectivity. Such evolution is evidenced by the change in molecular tilt angle observed with PEY NEXAFS starting from 150 °C (Figure 3) and by the film topography (Figure 4), evolving with thermal annealing from a clear fibrillar structure toward a much more interconnected layer. It may also be speculated that a similar improved coherence length in each crystalline direction with temperature, as measured on average in the film with GIWAXS, may also undergo at the top surface of the film.

It is worth noting that in the case of PNDI-SVS, high mobility values in the range of 2 cm^2 V^{-1} s^{-1} are achieved with a lower degree of orientational order with respect to PNDI2OD-T2, thus suggesting that substitution of thiophenes with electron-rich selenophenes results in more effective intermolecular charge transfer and that there may be room for further improvement of the electrical properties of PNDI-SVS through the enhancement of the film long-range orientational order.

3. Conclusions

We have reported the synthesis, thin film structure, and electronic properties of a novel electron-transporting NDI-copolymer, PNDI-SVS featuring a selenophene-vinyl-selenophene donor moiety, showing a reduced energy bandgap of 1.31 eV and a slightly lower lying LUMO level (−3.98 eV) with respect to the extensively studied PNDI2OD-T2 reference copolymer. PNDI-SVS, enables high-performance solution-processed OFETs, with optimized devices showing electron mobility of 2.4 cm^2 V^{-1} s^{-1} and a promising stability for ambient air operation, prior to any specific encapsulation, which is in any case required for applications. Its DOS is interestingly characterized by the superposition of two Gaussian functions, one shifted 0.1 eV with respect to the other yielding a relatively broad distribution, where the central and dominant one has a total number of states $N_{0,1} = 10^{21}$ cm^{-3} and width $\sigma_1 = 92$ meV, and the smaller one $N_{0,2} = 10^{18}$ cm^{-3} and $\sigma_2 = 161$ meV. While also the central Gaussian is broader than what can be extracted for the reference copolymer PNDI2OD-T2, electron mobility is conversely much improved, suggesting a possible spatial correlation in the DOS.

Through GIWAXS measurements, we evidenced a marked morphology evolution with annealing temperature treatments of PNDI-SVS thin films toward a more crystalline phase, where for temperatures above 180 °C a remarkable 3D crystal structure arises with the presence of several mixed index peaks. Molecular packing within the bulk is prevalently face-on up to

210 °C, while a clear realignment of the film toward edge-on packing occurs for higher temperatures. No apparent phase transition is present for temperatures below 250 °C, as we have evidenced that similar packing and morphology can be accessed both at high temperatures for a short processing time (250 °C, 20 min), and at low temperatures for a long time (130 °C, 24 h), where the main difference is observed only in the coherence lengths along all directions, indicating the strongly improved quality and size of crystallites for higher temperatures.

The FETs electrical characteristics show mobility of ≈2 cm^2 V^{-1} s^{-1} at an annealing temperature of 150 °C, clearly deviating from a simplistic explanation where the transport properties can be directly correlated with bulk sensitive GIWAXS measurements.

NEXAFS analysis of the topmost molecular layers, where charge accumulation mainly takes place, reveals a tendency toward edge-on molecular packing, even at low temperatures and in the as-cast film, consistently with AFM topography, indicating a fibrillar-like supramolecular morphology. This structural evidence is complemented by charge-modulation microscopy measurements, which reveal that mobile charge probe hundreds of nanometers wide orientational domains. Such domains are found to be very similar for devices that underwent very different processes, and in particular for those based on as-cast films on Cs_2CO_3, for films annealed at 120 °C and at 250 °C, all displaying a limited orientational order around 50%. On the one hand, such evidence suggests a possible further improvement of mobility with improved directional order, on the other, it indicates that improved transport properties above 150 °C are linked to a microscopic structural evolution at the top surface, as evidenced in NEXAFS and AFM, improving film interconnectivity thanks to a more efficient π-stacking within a fixed extension and order of orientational domains.

The achievement of high mobility with relatively low processing temperatures is a critical aspect to enable applications in flexible, large-area plastic electronics. We rationalize the good transport properties achieved at low temperature with the presence of a segregated polymer phase forming at the liquid–air interface, following different formation dynamics with respect to the bulk, which mostly presents an edge-on packing motif and where charge follows orientational domains rather insensitive to annealing conditions.

Further development in the field of high-performing semiconducting polymer FETs will be strongly influenced by the correct evaluation of the solid-state morphology and electronic properties of the sole fraction of molecules, the so-called "functional morphology", contributing to transport in FET devices, especially in polymer systems with highly localized carriers and elongated, fibril supramolecular structures, favoring the formation of directional domains.

4. Experimental Section

Materials and Characterization: All starting materials were purchased from Sigma-Aldrich (South Korea), TCI, and Alfa Aesar, and were used without further purification. Pd catalyst was purchased from Amicore. ^1H NMR spectra were recorded using a Bruker Avance 300 MHz and Bruker 500 FT-NMR spectrometer; chemical shifts (ppm) were reported with

www.MaterialsViews.com

ADVANCED
FUNCTIONAL
MATERIALS
www.afm-journal.de

FULL PAPER

tetramethylsilane as an internal standard. Fourier transform (FT)-IR spectra were recorded using a Bruker IFS66 spectrometer. TGA was performed under N_2 using a TA instrument 2050 TG analyzer. DSC was conducted under N_2 using a TA instrument DSC Q10, and both samples were heated at a rate of 10 °C min⁻¹. UV–vis spectra were measured using a Shimadzu UV-1065PC UV–vis spectrophotometer. The electrochemical properties of the materials were measured by cyclic voltammetry (CV) using Epsilon C3 in a 0.1 M solution of tetrabutyl ammonium perchlorate (TBAP) in chloroform. Molecular weights and polydispersities of the copolymers were determined by ACQUITY APC System with polystyrene standard calibration (solvent: chloroform).

Synthesis of 4,9-Dibromo-2,7-bis(2-Decyltetradecyl)benzo[lmn][3,8]-Phenanthroline-1,3,6,8(2H,7H)-Tetraone (NDI-Br₂) (1): The reaction followed the reported method.[69] 4,9-Dibromoisochromeno[6,5,4-*def*] isochromene-1,3,6,8-tetraone (NDA-Br₂) (10.00 g, 23.47 mmol) and 2-decyltetradecan-1-amine (20.75 g, 58.68 mmol) were added to 200 mL of acetic acid. The reaction mixture was refluxed under N_2 for 1 h. Then the reaction mixture was poured onto water and the resulting precipitate was filtered and washed with methanol. The crude product was purified via column chromatography over silica gel (eluent: dichloromethane/hexane = 1/1). NDI-Br₂ was obtained as a light yellow solid. Yield: 40% (10.36 g). ¹H NMR (300 MHz, CDCl₃, δ): 9.01 (s, 2H), 4.16–4.14 (t, 4H), 2.15–2.00 (m, 2H), 1.27 (m, 80H), 0.92–0.88 (t, 12H); ¹³C NMR (125 MHz, CDCl₃, δ): 163.81, 163.65, 141.79, 131.00, 130.38, 127.92, 126.71, 48.08, 39.10, 34.56, 34.55, 34.18, 32.66, 32.33, 32.31, 32.30, 32.28, 32.26, 32.23, 32.00, 31.98, 28.97, 25.34, 25.33, 16.76; IR (KBr, cm⁻¹): v = 3048, 2926, 2846, 1710, 1655.

Synthesis of Selenophene-2-Carbaldehyde (2): The reaction followed the reported method.[46] The crude product was purified via column chromatography over silica gel (eluent: dichloromethane/hexane = 1/9). Compound 2 was obtained as a yellow oil. Yield: 70% (8.49 g). ¹H NMR (300 MHz, CDCl₃, δ): 9.80 (s, 1H), 8.49 (d, 1H), 8.01 (dd, 1H), 7.47 (dd, 1H); ¹³C NMR (75 MHz, CDCl₃, δ): 184.36, 150.37, 141.12, 139.56, 130.86.

Synthesis of (E)-1,2-Di(selenophen-2-yl)Ethene (3): The reaction followed the reported method.[63] The crude product was purified via column chromatography over silica gel (eluent: dichloromethane/hexane = 1/5). Compound 3 was obtained as a yellow powder. Yield: 53% (4.06 g). ¹H NMR (300 MHz, CDCl₃, δ): 7.90–7.88 (dd, 2H), 7.25–7.23 (m, 4H), 7.05 (s, 2H). ¹³C NMR (75 MHz, CD₂Cl₂, δ): 148.29, 130.19, 129.03, 128.95, 125.04.

Synthesis of (E)-1,2-Bis(5-(trimethylstannyl)Selenophen-2-yl)Ethene (4): The reaction followed the reported method.[63] The crude solid was recrystallized from methanol to obtain (E)-1,2-bis(5-(trimethylstannyl)-selenophen-2-yl)ethene as yellow needles. Yield: 74% (2.02 g). ¹H NMR (300 MHz, CD₂Cl₂, δ): 7.96–7.95 (m, 2H), 7.46–7.44 (d, 2H), 7.04–7.00 (dd, 2H), 0.37 (s, 18H). ¹³C NMR (125 MHz, CD₂Cl₂, δ): 153.47, 145.03, 138.50, 129.91, 125.22, −8.34.

Synthesis of Poly[(E)-2,7-Bis(2-decyltetradecyl)-4-methyl-9-(5-(2-(5-methylselenophen-2-yl)vinyl)Selenophen-2-yl)Benzo[lmn][3,8]-Phenanthroline-1,3,6,8(2H,7H)-Tetraone] (PNDI-SVS): The polymer was prepared from a palladium-catalyzed Stille coupling reaction. 4,9-Dibromo-2,7-bis(2-decyltetradecyl)benzo[lmn][3,8]phenanthroline-1,3,6,8(2H,7H)-tetraone (NDI-Br₂) (0.50 g, 0.46 mmol) and (E)-1,2-bis(5-(trimethylstannyl)selenophen-2-yl)ethene (0.28 g, 0.46 mmol) were dissolved in dry chlorobenzene (7.5 mL). After degassing with nitrogen for 1 h, Pd₂(dba)₃ (8 mg) and P(o-Tol)₃ (11 mg) were added to the mixture and stirred for 48 h at 110 °C. 2-Bromothiophene and tributyl(thiophen-2-yl)stannane were added successively at a time interval of 6 h to end-cap the end groups. The polymer was precipitated in methanol. The crude polymer was collected by filtration and then purified by Soxhlet extractions with methanol, acetone, hexane, toluene, and chloroform, successively. The final product was obtained by precipitation in methanol and drying in vacuo. PNDI-SVS was obtained as a dark green solid. Yield: 97% (0.54 g). ¹H NMR (500 MHz, CDCl₃, δ): 8.80–8.46 (br, 2H), 7.93–7.20 (br, 6H), 4.12–4.10 (br, 4H), 1.98–1.87 (m, 2H), 1.25 (br, 80H), 0.87–0.86 (m, 12H).

Field-Effect Transistor Fabrication and Characterization: The Au/Ni (15 nm/3 nm thick) patterns used for the source and drain electrodes were fabricated using a conventional photolithography procedure on Corning Eagle 2000 glass substrates. Substrates were cleaned sequentially in an ultrasonic bath with de-ionized water, acetone, and iso-propanol and then baked at 110 °C. Au source and drain electrodes of some devices were treated with Cs₂CO₃ as an electron injection layer. The Cs₂CO₃ (Sigma-Aldrich) was dissolved in 2-ethoxyethanol and spin-coated in a N_2-purged glove box onto a patterned glass substrate with Au bottom contact electrodes. The substrates were thermally annealed at 120 °C for 30 min in an N_2-filled glove box. The conjugated polymer PNDI-SVS was dissolved in anhydrous chlorobenzene solvent to obtain a 12 mg mL⁻¹ solution. The semiconductor solutions were filtered with a 0.2 μm polytetrafluoroethylene syringe filter and spin coated at 2000 rpm for 60s in an N_2-filled glove box. The spin-coated PNDI-SVS films were thermally annealed at various temperatures from 120 to 250 °C for 20 min in the N_2-purged glove box. PMMA (M_W = 120 kD) was used as the dielectric without further purifications. PMMA was dissolved in n-butylacetate, spin-coated on the semiconducting polymer film and baked at 80 °C to remove residual solvent under N_2-purged atmosphere. The transistors were completed by depositing the top-gate electrodes (Al) via thermal evaporation using a metal shadow mask. Devices used in the ambient stability tests were placed in a controlled humidity atmosphere on the completion of the fabrication process. All FETs electrical characteristics were measured using HP 4156A in an N_2-filled glove box. The μ_{FET} and V_{Th} were calculated at the saturation region using gradual channel approximation equation.[81]

Preparation of Metal–Insulator–Semiconductor Capacitors for Determination of the Density of States: The MIS-capacitors were prepared with gold as the bottom injecting contact, defined by photolithography. PNDI-SVS was spin-coated from anhydrous chlorobenzene and annealed at 120 °C for 20 min. The PMMA dielectric was spin-coated on top of the semiconductor and aluminum was thermally deposited to form the gate electrode. Finally, the devices were annealed overnight at 130 °C. The CV characteristics of the MIS-capacitors were measured using an Agilent E4980A Precision LCR Meter. CV curves were fitted using a custom software developed to solve the nonlinear Poisson equation and to calculate the capacitance of the device at each applied voltage.[62]

GIWAXS measurements: GIWAXS measurements were carried out with a Dectris Pilatus 1 M detector. 11 or 18 keV (for the 250 and 130 °C 24 h annealed samples) highly collimated photons were aligned normal to the sample by using a photodiode. Angular steps of 0.01° were taken near the critical angle, which was determined as the angle of maximum scattered intensity. Each 2D scatter pattern was a result of a total of 3 s of exposure. Three 1 s exposures were taken at different detector positions to fill in the gaps between modules in the detector, and combined in the software. Correction of data onto momentum transfer axes and sector profiles was done using an altered version of NIKA.[82] Peak fitting was done using least squares multipeak fitting within Igor Pro. By identifying the scattering peaks, and fitting them with a log cubic empirical background function, we can monitor the crystallinity in the three major unit cell directions. Peak area is proportional to the number of molecular planes that participate in crystalline stacking and so the relative crystallinity within the thin film, while the peak width is an indication of the coherence length of that crystallinity and represents the size and quality of those crystals, and finally the location of the peak gives the d-spacing or the distance from one unit cell to the next along that direction.

NEXAFS measurements: NEXAFS measurements were conducted using X-rays produced by an elliptically polarized undulator and a 1200 lines/mm grating, producing highly polarized X-rays with a bandwidth of ≈0.1 eV across the measurement range. TEY was measured by monitoring the drain current to the sample, PEY was measured with a channeltron detector with a retarding voltage of ≈200 V, and FY was measured by a multichannel plate detector with a retarding field of 2600 V. Dark levels were measured and subtracted from the data, and double normalization was done using a gold mesh corrected by a

photodiode.[83] Peak fitting and tilt angle calculations were done using the Quick AS NEXAFS Tool.[84]

All tilt angles are calculated from a peak fit of structure at lower energies than 286 eV, which is in the π^* manifold, corresponding to transition dipole moments normal to the face of a conjugated core, along the direction of the carbon π orbitals. Thus, a tilt angle of 90° indicates that every TDM is perfectly in plane, and so all the conjugated faces are oriented perfectly edge-on to the substrate, while a tilt angle of 0° indicates perfectly face-on orientation. Because of the uniaxial alignment of spin-coated films, an unaligned film will have an average tilt angle of ≈54.7°. It is also impossible to determine through only a tilt angle measurement the distribution of local tilt angles within the film, but only the ensemble tilt angle. Thus, any fixed dihedral angle between backbone components will result in an average tilt angle between the tilt angles of each component. As opposed to GIWAXS, NEXAFS is sensitive to all molecules, regardless of them being in a crystalline or amorphous region.

GIWAXS and NEXAFS experiments were performed on the SAXS/WAXS[85] and Soft X-ray[86] beamlines at the Australian Synchrotron, Victoria, Australia.

Polarized charge Modulation Microscopy: The p-CMM data were collected with a homemade confocal microscope operating in transmission mode. The light source consisted of a supercontinuum laser (NKT Photonics, SuperK Extreme) monochromated by an acousto-optic modulator (NKT Photonics, SuperK Select) in the 500–1000 nm region with line widths between 2 and 5 nm. Laser polarization was controlled with a half-wave plate and a linear polarizer. The light was then focused on the sample with a 0.7 N.A. objective (S Plan Fluor60, Nikon) and collected by a second 0.75 N.A. objective (CFI Plan Apochromat VC 20, Nikon). The collected light was focused to the entrance of a multimodal glass fiber with a 50 µm core, acting as the confocal aperture. Detection was operated through a silicon photodetector (FDS100, Thorlabs). The signal was amplified by a transimpedance amplifier (DHPCA-100, Femto) and supplied both to a DAQ (to record the transmission signal, T) and to a lock-in amplifier (SR830 DSP, Stanford Research Systems) to retrieve the differential transmission data, ΔT. The system was run with homemade Labview software The OD values were obtained from T, as described in the Supporting Information, while the CMS data were calculated as $\Delta T/T$. The sample was kept in an inert atmosphere by fluxing nitrogen in a homemade chamber. The gate voltage of the transistor was sinusoidally modulated at 989 Hz between 20 and 60 V with a waveform generator (3390, Keithley) amplified by a high-voltage amplifier (WMA-300, Falco Systems), while the source and drain contacts were kept at short-circuit. Signal maps were collected by raster scanning the sample at 250 ms per pixel, with a lock-in integration time of 100 ms. All data were processed with Matlab software.

Supporting Information

Supporting Information is available from the Wiley Online Library or from the author.

Acknowledgements

[1] R. Noriega, J. Rivnay, K. Vandewal, F. P. V. Koch, N. Stingelin, P. Smith, M. F. Toney, A. Salleo, *Nat. Mater.* **2013**, *12*, 1038.

[2] H. Sirringhaus, *Adv. Mater.* **2014**, *26*, 1319.

[3] S. G. Bucella, A. Luzio, E. Gann, L. Thomsen, C. R. McNeill, G. Pace, A. Perinot, Z. Chen, A. Facchetti, M. Caironi, *Nat. Commun.* **2015**, *6*, 8394.

[4] C. Liu, Y. Xu, Y.-Y. Noh, *Mater. Today* **2015**, *18*, 79.

[5] D. Fazzi, M. Caironi, *Phys. Chem. Chem. Phys.* **2015**, *17*, 8573.

[6] D. Natali, M. Caironi, *Adv. Mater.* **2012**, *24*, 1357.

[7] D. Khim, Y. Xu, K.-J. Baeg, M. Kang, W.-T. Park, S.-H. Lee, I.-B. Kim, J. Kim, D.-Y. Kim, C. Liu, Y.-Y. Noh, *Adv. Mater.* **2016**, *28*, 518.

[8] S. R. Forrest, *Nature* **2004**, *428*, 911.

[9] R. R. Søndergaard, M. Hösel, F. C. Krebs, *J. Polym. Sci., Part B: Polym. Phys.* **2013**, *51*, 16.

[10] S. G. Bucella, G. Nava, K. C. Vishunubhatla, M. Caironi, *Org. Electron.* **2013**, *14*, 2249.

[11] F. C. Krebs, J. Fyenbo, M. Jorgensen, *J. Mater. Chem.* **2010**, *20*, 8994.

[12] G. Dell'Erba, A. Luzio, D. Natali, J. Kim, D. Khim, D.-Y. Kim, Y.-Y. Noh, M. Caironi, *Appl. Phys. Lett.* **2014**, *104*, 153303.

[13] G. Azzellino, A. Grimoldi, M. Binda, M. Caironi, D. Natali, M. Sampietro, *Adv. Mater.* **2013**, *25*, 6829.

[14] G. Pace, A. Grimoldi, D. Natali, M. Sampietro, J. E. Coughlin, G. C. Bazan, M. Caironi, *Adv. Mater.* **2014**, *26*, 6773.

[15] K.-J. Baeg, M. Caironi, Y.-Y. Noh, *Adv. Mater.* **2013**, *25*, 4210.

[16] G. Dell'Erba, A. Perinot, A. Grimoldi, D. Natali, M. Caironi, *Semicond. Sci. Technol.* **2015**, *30*, 104005.

[17] C. M. Lochner, Y. Khan, A. Pierre, A. C. Arias, *Nat. Commun.* **2014**, *5*, 5745.

[18] G. H. Gelinck, A. Kumar, D. Moet, J.-L. van der Steen, U. Shafique, P. E. Malinowski, K. Myny, B. P. Rand, M. Simon, W. Rütten, A. Douglas, J. Jorritsma, P. Heremans, R. Andriessen, *Org. Electron.* **2013**, *14*, 2602.

[19] B. K. C. Kjellander, W. T. T. Smaal, K. Myny, J. Genoe, W. Dehaene, P. Heremans, G. H. Gelinck, *Org. Electron.* **2013**, *14*, 768.

[20] M. Kaltenbrunner, T. Sekitani, J. Reeder, T. Yokota, K. Kuribara, T. Tokuhara, M. Drack, R. Schwodiauer, I. Graz, S. Bauer-Gonogea, S. Bauer, T. Someya, *Nature* **2013**, *499*, 458.

[21] Y. Yamashita, F. Hinkel, T. Marszalek, W. Zajaczkowski, W. Pisula, M. Baumgarten, H. Matsui, K. Müllen, J. Takeya, *Chem. Mater.* **2016**, *28*, 420.

[22] I. Kang, H.-J. Yun, D. S. Chung, S.-K. Kwon, Y.-H. Kim, *J. Am. Chem. Soc.* **2013**, *135*, 14896.

[23] G. Kim, S.-J. Kang, G. K. Dutta, Y.-K. Han, T. J. Shin, Y.-Y. Noh, C. Yang, *J. Am. Chem. Soc.* **2014**, *136*, 9477.

[24] J. Li, Y. Zhao, H. S. Tan, Y. Guo, C.-A. Di, G. Yu, Y. Liu, M. Lin, S. H. Lim, Y. Zhou, H. Su, B. S. Ong, *Sci. Rep.* **2012**, *2*, 754.

[25] C. Luo, A. K. Kyaw, L. A. Perez, S. Patel, M. Wang, B. Grimm, G. C. Bazan, E. J. Kramer, A. J. Heeger, *Nano Lett.* **2014**, *14*, 2764.

[26] J. Yao, C. Yu, Z. Liu, H. Luo, Y. Yang, G. Zhang, D. Zhang, *J. Am. Chem. Soc.* **2016**, *138*, 173.

[27] C. B. Nielsen, M. Turbiez, I. McCulloch, *Adv. Mater.* **2013**, *25*, 1859.

[28] R. Stalder, J. Mei, K. R. Graham, L. A. Estrada, J. R. Reynolds, *Chem. Mater.* **2014**, *26*, 664.

[29] T. Lei, J.-Y. Wang, J. Pei, *Acc. Chem. Res.* **2014**, *47*, 1117.

[30] W. Zhang, J. Smith, S. E. Watkins, R. Gysel, M. McGehee, A. Salleo, J. Kirkpatrick, S. Ashraf, T. Anthopoulos, M. Heeney, I. McCulloch, *J. Am. Chem. Soc.* **2010**, *132*, 11437.

www.MaterialsViews.com

ADVANCED
FUNCTIONAL
MATERIALS
www.afm-journal.de

FULL PAPER

[31] A. Luzio, D. Fazzi, F. Nübling, R. Matsidik, A. Straub, H. Komber, E. Giussani, S. E. Watkins, M. Barbatti, W. Thiel, E. Gann, L. Thomsen, C. R. McNeill, M. Caironi, M. Sommer, *Chem. Mater.* **2014**, *26*, 6233.

[32] H. J. Yun, S. J. Kang, Y. Xu, S. O. Kim, Y. H. Kim, Y. Y. Noh, S. K. Kwon, *Adv. Mater.* **2014**, *26*, 7300.

[33] B. Sun, W. Hong, Z. Yan, H. Aziz, Y. Li, *Adv. Mater.* **2014**, *26*, 2636.

[34] A. Lv, S. R. Puniredd, J. Zhang, Z. Li, H. Zhu, W. Jiang, H. Dong, Y. He, L. Jiang, Y. Li, W. Pisula, Q. Meng, W. Hu, Z. Wang, *Adv. Mater.* **2012**, *24*, 2626.

[35] C. Kanimozhi, N. Yaacobi-Gross, K. W. Chou, A. Amassian, T. D. Anthopoulos, S. Patil, *J. Am. Chem. Soc.* **2012**, *134*, 16532.

[36] L. Zhang, N. S. Colella, F. Liu, S. Trahan, J. K. Baral, H. H. Winter, S. C. B. Mannsfeld, A. L. Briseno, *J. Am. Chem. Soc.* **2013**, *135*, 844.

[37] H. Usta, A. Facchetti, T. J. Marks, *Acc. Chem. Res.* **2011**, *44*, 501.

[38] H. Yan, Z. Chen, Y. Zheng, C. Newman, J. R. Quinn, F. Dotz, M. Kastler, A. Facchetti, *Nature* **2009**, *457*, 679.

[39] V. D'Innocenzo, A. Luzio, A. Petrozza, D. Fazzi, M. Caironi, *Adv. Funct. Mater.* **2014**, *24*, 5584.

[40] V. Lemaur, L. Muccioli, C. Zannoni, D. Beljonne, R. Lazzaroni, J. Cornil, Y. Olivier, *Macromolecules* **2013**, *46*, 8171.

[41] C. Caddeo, D. Fazzi, M. Caironi, A. Mattoni, *J. Phys. Chem. B* **2014**, *118*, 12556.

[42] R. Kim, P. S. K. Amegadze, I. Kang, H.-J. Yun, Y.-Y. Noh, S.-K. Kwon, Y.-H. Kim, *Adv. Funct. Mater.* **2013**, *23*, 5719.

[43] M. Heeney, W. Zhang, D. J. Crouch, M. L. Chabinyc, S. Gordeyev, R. Hamilton, S. J. Higgins, I. McCulloch, P. J. Skabara, D. Sparrowe, S. Tierney, *Chem. Commun.* **2007**, 5061.

[44] D. J. Crouch, P. J. Skabara, J. E. Lohr, J. J. W. McDouall, M. Heeney, I. McCulloch, D. Sparrowe, M. Shkunov, S. J. Coles, P. N. Horton, M. B. Hursthouse, *Chem. Mater.* **2005**, *17*, 6567.

[45] D. Khim, W.-H. Lee, K.-J. Baeg, D.-Y. Kim, I.-N. Kang, Y.-Y. Noh, *J. Mater. Chem.* **2012**, *22*, 12774.

[46] I. Kang, T. K. An, J. A. Hong, H. J. Yun, R. Kim, D. S. Chung, C. E. Park, Y. H. Kim, S. K. Kwon, *Adv. Mater.* **2013**, *25*, 524.

[47] M. Shahid, T. McCarthy-Ward, J. Labram, S. Rossbauer, E. B. Domingo, S. E. Watkins, N. Stingelin, T. D. Anthopoulos, M. Heeney, *Chem. Sci.* **2012**, *3*, 181.

[48] J. Lee, A. R. Han, J. Kim, Y. Kim, J. H. Oh, C. Yang, *J. Am. Chem. Soc.* **2012**, *134*, 20713.

[49] H. Kong, Y. K. Jung, N. S. Cho, I.-N. Kang, J.-H. Park, S. Cho, H.-K. Shim, *Chem. Mater.* **2009**, *21*, 2650.

[50] B. Kim, H. R. Yeom, M. H. Yun, J. Y. Kim, C. Yang, *Macromolecules* **2012**, *45*, 8658.

[51] T. Earmme, Y.-J. Hwang, N. M. Murari, S. Subramaniyan, S. A. Jenekhe, *J. Am. Chem. Soc.* **2013**, *135*, 14960.

[52] Y.-J. Hwang, N. M. Murari, S. A. Jenekhe, *Polym. Chem.* **2013**, *4*, 3187.

[53] M. Brinkmann, L. Hartmann, L. Biniek, K. Tremel, N. Kayunkid, *Macromol. Rapid Commun.* **2014**, *35*, 9.

[54] H.-R. Tseng, H. Phan, C. Luo, M. Wang, L. A. Perez, S. N. Patel, L. Ying, E. J. Kramer, T.-Q. Nguyen, G. C. Bazan, A. J. Heeger, *Adv. Mater.* **2014**, *26*, 2993.

[55] R. Joseph Kline, M. D. McGehee, M. F. Toney, *Nat. Mater.* **2006**, *5*, 222.

[56] K. Tremel, F. S. U. Fischer, N. Kayunkid, R. Di Pietro, R. Tkachov, A. Kiriy, D. Neher, S. Ludwigs, M. Brinkmann, *Adv. Energy Mater.* **2014**, *4*, 1301659.

[57] L. Biniek, N. Leclerc, T. Heiser, R. Bechara, M. Brinkmann, *Macromolecules* **2013**, *46*, 4014.

[58] R. Matsidik, H. Komber, A. Luzio, M. Caironi, M. Sommer, *J. Am. Chem. Soc.* **2015**, *137*, 6705.

[59] N.-K. Kim, S.-Y. Jang, G. Pace, M. Caironi, W.-T. Park, D. Khim, J. Kim, D.-Y. Kim, Y.-Y. Noh, *Chem. Mater.* **2015**, *27*, 8345.

[60] N. Martino, D. Fazzi, C. Sciascia, A. Luzio, M. R. Antognazza, M. Caironi, *ACS Nano* **2014**, *8*, 5968.

[61] C. Sciascia, N. Martino, T. Schuettfort, B. Watts, G. Grancini, M. R. Antognazza, M. Zavelani-Rossi, C. R. McNeill, M. Caironi, *Adv. Mater.* **2011**, *23*, 5086.

[62] F. Maddalena, C. de Falco, M. Caironi, D. Natali, *Org. Electron.* **2015**, *17*, 304.

[63] B. A. Jones, A. Facchetti, M. R. Wasielewski, T. J. Marks, *J. Am. Chem. Soc.* **2007**, *129*, 15259.

[64] M. Caironi, C. Newman, J. R. Moore, D. Natali, H. Yan, A. Facchetti, H. Sirringhaus, *Appl. Phys. Lett.* **2010**, *96*, 183303.

[65] Z. Chen, Y. Zheng, H. Yan, A. Facchetti, *J. Am. Chem. Soc.* **2008**, *131*, 8.

[66] D. Fazzi, M. Caironi, C. Castiglioni, *J. Am. Chem. Soc.* **2011**, *133*, 47.

[67] A. Luzio, D. Fazzi, D. Natali, E. Giussani, K.-J. Baeg, Z. Chen, Y.-Y. Noh, A. Facchetti, M. Caironi, *Adv. Funct. Mater.* **2014**, *24*, 1151.

[68] E. Giussani, D. Fazzi, L. Brambilla, M. Caironi, C. Castiglioni, *Macromolecules* **2013**, *46*, 2658.

[69] R. Kim, P. S. K. Amegadze, I. Kang, H.-J. Yun, Y.-Y. Noh, S.-K. Kwon, Y.-H. Kim, *Adv. Funct. Mater.* **2013**, *23*, 5719.

[70] L. A. Perez, P. Zalar, L. Ying, K. Schmidt, M. F. Toney, T.-Q. Nguyen, G. C. Bazan, E. J. Kramer, *Macromolecules* **2014**, *47*, 1403.

[71] E. Gann, M. Caironi, Y.-Y. Noh, Y.-H. Kim, C. R. McNeill, unpublished.

[72] T. Schuettfort, L. Thomsen, C. R. McNeill, *J. Am. Chem. Soc.* **2013**, *135*, 1092.

[73] K.-J. Baeg, J. Kim, D. Khim, M. Caironi, D.-Y. Kim, I.-K. You, J. R. Quinn, A. Facchetti, Y.-Y. Noh, *ACS Appl. Mater. Interfaces* **2011**, *3*, 3205.

[74] C. Liu, J. Jang, Y. Xu, H.-J. Kim, D. Khim, W.-T. Park, Y.-Y. Noh, J.-J. Kim, *Adv. Funct. Mater.* **2015**, *25*, 758.

[75] T. Kurosawa, Y.-C. Chiu, Y. Zhou, X. Gu, W.-C. Chen, Z. Bao, *Adv. Funct. Mater.* **2015**, *6*, 1261.

[76] R. Di Pietro, D. Fazzi, T. B. Kehoe, H. Sirringhaus, *J. Am. Chem. Soc.* **2012**, *134*, 14877.

[77] R. Coehoorn, P. A. Bobbert, *Phys. Status Solidi A* **2012**, *209*, 2354.

[78] C. J. Takacs, N. D. Treat, S. Krämer, Z. Chen, A. Facchetti, M. L. Chabinyc, A. J. Heeger, *Nano Lett.* **2013**, *13*, 2522.

[79] X. Zhang, H. Bronstein, A. J. Kronemeijer, J. Smith, Y. Kim, R. J. Kline, L. J. Richter, T. D. Anthopoulos, H. Sirringhaus, K. Song, M. Heeney, W. Zhang, I. McCulloch, D. M. DeLongchamp, *Nat. Commun.* **2013**, *4*, 2238.

[80] A. Luzio, L. Criante, V. D'Innocenzo, M. Caironi, *Sci. Rep.* **2013**, *3*, 3425.

[81] S. M. Sze, K. K. Ng, *Physics of Semiconductor Devices*, 3rd ed., John Wiley & Sons, Inc., Hoboken, NJ, USA **2006**.

[82] J. Ilavsky, *J. Appl. Crystallogr.* **2012**, *45*, 324.

[83] B. Watts, L. Thomsen, P. C. Dastoor, *J. Electron. Spectrosc. Relat. Phenom.* **2006**, *151*, 105.

[84] E. Gann, C. R. McNeill, A. Tadich, B. C. C. Cowie, L. Thomsen, *J. Synchrotron Radiat.* **2016**, *23*, 374.

[85] N. M. Kirby, S. T. Mudie, A. M. Hawley, D. J. Cookson, H. D. T. Mertens, N. Cowieson, V. Samardzic-Boban, *J. Appl. Crystallogr.* **2013**, *46*, 1670.

[86] B. C. C. Cowie, A. Tadich, L. Thomsen, *AIP Conf. Proc.* **2010**, *1234*, 307.